Last Updated: 07/31/2008

Winter Atmosphere – Mixed Layer Ocean Response to Geostrophic Ocean Heat Transport Variations along the Kuroshio Current Extension

Young-Oh Kwon[1], Clara Deser[2], and Christophe Cassou[3]

1: Woods Hole Oceanographic Institution, Woods Hole, Massachusetts, USA

2: National Center for Atmospheric Research, Boulder, Colorado, USA

3: CNRS-CERFACS, Toulouse, France

Submitted to the Journal of Climate

August 1, 2008

Corresponding Author Address: Dr. Young-Oh Kwon, Physical Oceanography Department, Woods Hole Oceanographic Institution, Clark 320A, MS#21, Woods Hole, MA 02543.

E-mail: yokwon@whoi.edu

Abstract

The winter response of the coupled atmosphere-ocean mixed layer system to anomalous geostrophic ocean heat flux convergence (OHFC) in the Kuroshio Extension is investigated by means of experiments with an atmospheric general circulation model coupled to an entraining ocean mixed layer model. In addition to the direct response, interaction with the tropics and the role of the extra-tropical ocean mixed layer are addressed. The direct coupled ocean mixed layer - atmospheric circulation response to a positive OHFC anomaly in the Kuroshio Extension consists of anomalous positive SST along the Kuroshio Extension and a baroclinic atmospheric response characterized by a low-level trough and upper-level ridge over the north Pacific. The low-level component of this atmospheric circulation response is weaker in the case without coupling to an extratropical ocean mixed layer compared to the case with coupling, especially in late winter. The inclusion of an interactive mixed layer in the tropics modifies the direct coupled atmospheric response as a result of a northward displacement of the Pacific Inter-Tropical Convergence Zone which drives an equivalent barotropic anomalous ridge over the north Pacific. Although the tropically-driven component of the north Pacific atmospheric circulation response is comparable to the direct response in terms of sea level pressure amplitude, it is less important in terms of wind stress curl amplitude due to the mitigating effect of the relatively broad spatial scale of the tropically-forced atmospheric teleconnection.

1. Introduction

The ocean carries approximately half of the net poleward heat transport at low latitudes, of which approximately 70% is released to the atmosphere between 25° and 45° N (Trenberth and Caron 2001; Wunsch 2005). The heat transfer from ocean to atmosphere, mainly in the form of latent and sensible energy fluxes with maximum amplitude during winter, is concentrated near the western boundary current region of each basin, i.e. the Kuroshio in the North Pacific and the Gulf Stream in the North Atlantic. Thus, the western boundary current regions and their eastward extensions serve as conduits for oceanic forcing of the atmosphere, both in a climatological mean sense and in terms of interannual and longer time scale variability (Tanimoto et al. 2003; Kelly and Dong 2004).

The response of the large-scale atmospheric circulation to ocean heat transport variations by the western boundary currents is not well understood, although it is a key component in theories of decadal-scale extra-tropical atmosphere-ocean variability. In particular, the strength and pattern of the atmospheric circulation response to extra-tropical sea surface temperature (SST) anomalies determines whether such decadal-scale variability is a result of mutual coupling between the ocean and atmosphere (Latif and Barnett 1996; Neelin and Weng 1999; Marshall et al. 2001; Pierce et al. 2001; Kwon and Deser 2007; Qiu et al. 2007) or an ocean-only mode (Frankignoul et al. 1997; Saravanan and McWilliams 1998; Cessi and Primeau 2001; Qiu 2003; Berloff et al. 2007).

The response of the atmosphere to extratropical SST variations is difficult to discern in observations due to the dominance of atmospheric forcing of SST anomalies (Frankignoul, 1983; Cayan, 1992; Deser and Timlin, 1997). Thus, a common approach

for studying the atmospheric response to extra-tropical SST anomalies has been to drive an atmospheric general circulation model (AGCM) with prescribed SST anomalies (see the review by Kushnir et al. 2002). However, the results diverge greatly among different modelling studies. Progress made in the past decade suggests that the diverse equilibrium atmospheric responses among different SST-specified AGCM studies can be attributed in part to differing sensitivity of transient eddy feedbacks (Peng et al. 1997; Peng and Whitaker 1999) and structure of the models' internal variability (Peng and Robinson 2001; Deser et al. 2004b). Linear model studies predict downstream low pressure anomalies at sea-level with a baroclinic vertical structure in response to shallow positive diabatic heating anomalies (Hoskins and Karoly 1981; Hendon and Hartman 1982). This so-called warm-low equilibrium response is associated with the anomalous northerly low-level wind balancing the imposed anomalous diabatic heating. However, nonlinear transient eddy feedbacks may substantially modify the linear response and produce an equivalent barotropic downstream high response (e.g. Peng and Whitaker 1999; Deser et al. 2007).

Several recent studies have noted the limitation of AGCM experiments with specified SST anomalies (e.g. Kumar and Hoerling 1998; Bretherton and Battisti 2000; Yulaeva et al. 2001; Sutton and Mathieu 2002). The experiments in which SSTs are not allowed to respond to changes in atmospheric circulation can produce misleading results, since the SST anomalies should result from the imbalance between the net heat flux across the air-sea interface and the lateral convergence of heat into the ocean mixed layer. One way to provide a more realistic assessment of the ocean's role in climate variability on interannual to multi-decadal timescales is to use a model configuration in which the

atmosphere is coupled to an ocean mixed layer with prescribed ocean heat transport variations due to dynamical processes not included in the ocean mixed layer model. In this configuration, SST and surface heat flux anomalies reflect to a greater degree the true two-way coupling between the atmosphere and the ocean mixed layer.

Two pioneering studies, one for the North Pacific (Yulaeva et al. 2001) and the other for the North Atlantic (Sutton and Mathieu 2002), have applied this approach. Both studies used idealized forms of ocean heat flux convergence (OHFC) anomalies due to lack of adequate observational estimates, and both employed AGCMs coupled to a non-entraining slab ocean mixed layer model. In the case of Sutton and Mathieu (2002), a 50 m fixed mixed layer depth (MLD) was used for the ocean mixed layer model with a prescribed seasonally-varying OHFC anomaly; while in the case of Yulaeva et al. (2001), a seasonally-varying MLD with a prescribed constant OHFC anomaly was used. Neither study included the process of entrainment whereby thermal anomalies from beneath the mixed layer are brought into the mixed layer. Both experiments were run with constant forcing for a period of 10 years and the atmospheric and SST distributions compared to control runs in which the OHFC anomaly was set to zero. The winter atmospheric circulation response in the study of Yulaeva et al. (2001) consisted of an equivalent barotropic low downstream of anomalously warm SST induced by lateral OHFC in the Kuroshio Extension. Sutton and Mathieu (2002) also reported a downstream equivalent barotropic low pressure response to anomalous OHFC in the Gulf Stream region.

Liu and Wu (2004) compared four approaches for investigating the atmospheric response to SST anomalies in the Kuroshio Extension region: (1) specified SST anomalies in an AGCM, (2) specified surface air-sea heat flux anomalies in an AGCM,

(3) specified ocean temperature anomalies in the upper 200 m as initial conditions to a fully coupled ocean-atmosphere GCM, and (4) as in (3) but allowing only thermal coupling. The specified SST anomaly experiment produced a downstream equivalent barotropic high-pressure response to a positive SST anomaly, while the air-sea heat flux anomaly experiment produced a downstream equivalent barotropic low response. The fully coupled experiment produced an equivalent barotropic high pressure response which they concluded was a combination of the responses in cases 1) and 2) above. The thermally coupled experiment produced a similar response to that of the fully coupled experiment but with about half the magnitude. However, their approach with specified surface air-sea heat flux anomaly could have the same limitation as the specified SST anomaly experiment, since the surface air-sea heat flux should result from the imbalance between the heat flux convergences in the lower atmosphere and the upper ocean. Thus, their surface air-sea heat flux specified experiments may not be equivalent to Sutton and Mathieu (2002) and Yulaeva et al. (2001) who specified the lateral OHFC anomalies and allowed SST and surface air-sea heat flux to be determined prognostically. On the other hand, the thermally coupled experiment with initial upper ocean temperature anomalies is more in line with the experimental design of Sutton and Mathieu (2002) and Yulaeva et al. (2001).

A subsequent study by Liu et al. (2007) explored further the fully coupled model approach, specifying uniform initial ocean temperature anomalies throughout the upper 560 m in the Kuroshio Extension of the coupled general circulation model and performed a 160-member ensemble of 4-year integrations. The results show that the subsurface ocean temperature anomalies re-emerged every winter despite the rapid and continuous

erosion of the initial thermal anomalies. They reported distinct atmospheric responses for early and late winter as in Peng et al. (1997). In November-January, the warm SST anomalies were accompanied by an equivalent barotropic ridge over the North Pacific and downstream wave train resembling the Pacific-North America (PNA) pattern (Wallace and Gutzler 1981). On the other hand, the atmospheric response in February-April was significantly weaker than that in November-January, with a baroclinic warm-low structure although the SST anomalies remained similar to those in early winter. They briefly speculated that the different responses in early and late winter may be due to the different background atmospheric state as suggested by Peng et al. (1997). A summary of the various studies cited above is given Table 1.

Kwon and Deser (2007) examined decadal variability in the North Pacific from a 650-year control integration of Community Climate System Model version 2 (CCSM2), a coupled general circulation model. Geostrophic OHFC variations in the Kuroshio Extension and the associated wind stress curl response were found to play key roles in the decadal (15-20 yr) coupled atmosphere-ocean oscillation. The wind stress curl response to the OHFC anomalies in CCSM2 was diagnosed empirically using linear regression analysis, supported with preliminary results from additional experiments with the atmospheric model component of CCSM2.

In this paper, we provide an in-depth analysis of the preliminary results on the atmospheric circulation response to OHFC anomalies in the Kuroshio Extension shown in Kwon and Deser (2007). In particular, we systematically compare the responses using the standard "specified SST" approach with the alternative "specified OHFC" approach. In order to understand the atmospheric response in the fully coupled system of CCSM2,

we retain the component models of CCSM2 as much as possible to ensure consistency between the CCSM2 and the simplified experiments. Specifically, we employ the atmospheric model component of CCSM2 for the "specified SST" experiments, and a simplified coupled model consisting of the atmospheric model component of CCSM2 coupled to an entraining ocean mixed layer model for the "specified OHFC" integrations. Decadal variations in OHFC along the Kuroshio Extension diagnosed from the CCSM2 are prescribed in the simplified coupled model experiments. The resulting SST anomalies are then specified in the atmospheric GCM experiments. Interaction of the atmospheric response over the North Pacific with the tropics is also systematically examined by comparing the simplified coupled model experiments with and without an interactive tropical ocean. Section 2 describes the model and experiment design. Results are presented in section 3 and discussed in section 4. Conclusions are presented in section 5.

2. Model Experiments

a. Coupled model : CMLM

The coupled model used in this study consists of an atmospheric general circulation model, a mixed layer ocean model, a thermodynamic sea-ice model and a land model (Cassou et al. 2007). The coupled model has almost identical atmospheric and land components as the CCSM2 (Kiehl and Gent 2004), while the ocean component is greatly simplified, and the sea-ice component retains only the thermodynamic portion of that in CCSM2. The atmospheric component model is the Community Atmospheric Model version 2 (CAM2) (Kiehl and Gent 2004), which has T42 horizontal resolution (= about 2.8° latitude by 2.8° longitude) and 26 vertical levels using a hybrid coordinate. The land

surface and the sea-ice components are the Community Land Model (CLM2) (Bonan et al. 2002) and the thermodynamic component of the Community Sea-Ice Model (CSIM4) (Briegleb et al. 2004), respectively. Ocean, sea-ice, and land models are all aligned with the atmospheric model grid.

The ocean component is an entraining mixed layer model (MLM), which is an array of independent single column multi-layer models with explicit mixed layer physics. The MLD is calculated prognostically for each time step based on Gaspar (1988)'s formulation as implemented by Alexander and Deser (1995). In the present study we use a version of the MLM modified by Cassou et al. (2007), which has 36 vertical layers in the upper 1500 m with 15 layers in the upper 100 m. The MLM allows us to specify the OHFC anomalies into multiple vertical layers of the upper ocean and also to examine the role of entrainment.

The climatological mean surface heat flux correction and salt flux correction are applied to account for missing physics in the MLM such as ocean heat transport by the mean currents and diffusion, as well as the model biases in the surface fluxes at the atmosphere-ocean boundary to a lesser extent. Note that Ekman transport is not included in the version of MLM used in this study. Hereafter, the coupled model is referred as CMLM. The reader is referred to Cassou et al. (2007) for further description of the CMLM.

b. CMLM control integration

The 150-year control integration of CMLM (*hereafter* CMLM-C) from Cassou et al. (2007) is used as a baseline experiment for comparison with the perturbation integrations.

The control integration, with the inclusion of flux corrections, produces a reasonable climatology as assessed in detail by Cassou et al. (2007). Figures S1 and S2 in the web supplement (http://www.cgd.ucar.edu/cas/cdeser/CMLM_supfig.html) provide additional comparisons among the CMLM, CCSM2 control integration, and observations. The main deficiency of the CMLM is the weaker year-to-year variability of SST over the North Pacific compared to that in CCSM2 and observations (maximum rms values ~ 0.5°C in CMLM compared to 0.8 °C in CCSM and 0.9°C in observations, excluding the region directly east of Japan). This may be due in part to the absence of lateral ocean dynamics in the MLM. Atmospheric variability is well simulated in CMLM compared to observations and CCSM2, including the intensity and location of the storm track over the North Pacific.

c. CMLM perturbation integrations

To investigate the coupled atmosphere – ocean mixed layer response to ocean heat transport variations, perturbation experiments are designed with additional decadal geostrophic OHFC anomalies in the Kuroshio Extension (35-45°N, 140-180°E) specified in the upper 1000 m of the CMLM. Two 100-year long perturbation integrations are performed with identical design except for the treatment of the tropical oceans. The first perturbation integration has the interactive MLM only in the extra-tropics (north of 20°N and south of 20°S) to isolate the response to the local anomalous OHFC forcing in the North Pacific. The climatological mean SST from the CMLM-C is specified in the tropics. The second perturbation integration has the interactive MLM over the entire global ocean including the tropics. Hereafter, the first and second perturbation integrations are referred

as CMLM-E and CMLM-G, respectively, where E stands for extra-tropics and G stands for global.

The decadal geostrophic OHFC anomalies are diagnosed from years 350-999 of the CCSM2 control integration (Kwon and Deser 2007). The anomalies for each month are calculated as the root-mean-square of 10-year low-pass filtered time series of the corresponding month's geostrophic OHFC. For example, January values for the 650 year period are first 10-year low-pass filtered and then the root-mean-square of the filtered time series is assigned as the January decadal anomaly. The decadal anomalies are calculated independently for each (longitude, latitude, depth) point. Then the repeating annual cycle of the anomalies are specified in CMLM. The Ekman OHFC has been removed from the total OHFC to retain only the geostrophic component, where we have assumed that the total Ekman OHFC is distributed uniformly throughout the mixed layer.

The distribution of specified geostrophic OHFC anomalies in the upper 10 m in March is shown in Fig. 1. Values are about 4.2 W m^{-2} on average in the Kuroshio Extension, with maximum amplitudes up to 15 W m^{-2} along 40°N near the coast of Japan (Fig. 1a). Note that we have specified only geostrophic OHFC anomalies in the domain confined to the Kuroshio Extension (35-45°N, 140-180°E) to ensure an appropriate oceanic forcing based on the analysis of CCSM2 by Kwon and Deser (2007). Spatial distributions in March are representative of those throughout the year with modulation of amplitude as shown in Fig. 1b. The average anomalies in the upper 10 m are maximum in February (=4.6 W m^{-2}) and minimum in September (=2.2 W m^{-2}). The geostrophic OHFC anomalies have significant magnitude beneath the climatological mean MLD (shown as the dashed lines in Fig. 1b-d). The vertical sections along 40°N and 150°E show

maximum amplitudes at the surface along 40°N near the coast of Japan and a gradual decrease with depth and distance from the maximum amplitude region (Fig. 1c-d).

A few observational estimates of geostrophic OHFC anomalies have been reported against which our estimates from CCSM2 may be compared. Qiu (2000) estimated January-March average non-seasonal geostrophic OHFC anomalies in the Kuroshio Extension to be about 5×10^{-8} ºC s^{-1}. Qiu (2000)'s estimate is based on the surface geostrophic velocity from sea surface height measurements of satellite altimetry during 1993-1999. Vivier et al. (2002) estimated non-seasonal lateral (geostrophic + Ekman) OHFC anomalies in the Kuroshio Extension to be about 2×10^{-8} ºC s^{-1}. They used a 3-dimensional advection-diffusion ocean model with specified geostrophic and Ekman velocities estimated from satellite altimetry measurements and wind stress from the NCEP-NCAR Reanalysis (Kalnay et al. 1996). By assimilating observed SST and subsurface temperature data into a simple upper-ocean mixed layer model for 1970-2000, Kelly (2004) estimated non-seasonal root-mean-square of lateral OHFC anomalies in the Kuroshio Extension and its recirculation gyre to be 9 W m^{-2} (~0.8×10^{-8} ºC s^{-1}) for the upper 300 m. Both Vivier et al. (2002) and Kelly (2004)'s estimates are not just for the winter months, but for the entire year. Thus, the geostrophic OHFC anomalies from CCSM2 are consistent with, albeit somewhat larger than, previous estimates based on the available observations.

The equilibrium responses of CMLM-E and CMLM-G are examined by computing the differences between the mean of the 100-year perturbation integrations and the mean of the 150-year control integration CMLM-C. The statistical significance of the responses at the 95% level is determined by Student's t-test. Each year is considered as independent,

so that the perturbation integrations and the control integration are considered as ensembles of 100 and 150 members, respectively. This assumption does not strictly hold since the re-emergence mechanism (Alexander et al. 1999) may provide some year-to-year persistence. Therefore, the robustness of the response is also evaluated by comparing sub-samples of the model output (e.g., first vs. second half, odd vs. even years). Overall, consistent results are found for the sub-sampled years (not shown).

d. Specified SST experiments

In addition to the coupled model experiments, we have conducted specified SST experiments with CAM2 using SSTs from the CMLM experiments. This SST-specified configuration is the traditional method for examining the atmospheric response to SST anomalies as discussed above. To ensure an appropriate comparison with the response in CMLM-E to the anomalous OHFC, a 150-year stand-alone CAM2 control integration (*hereafter* AGCM-C) is first performed with climatological mean annual cycle of SST and sea-ice concentration from the CMLM-C specified as the boundary condition. The annual cycle of the equilibrium SST responses of CMLM-E in the Kuroshio Extension (35-45°N, 140-180°E) is then added as anomalies to the SST boundary condition of AGCM-C in another 100-year stand-alone CAM2 perturbation integration (*hereafter* AGCM-E). The equilibrium response for the stand-alone CAM2 perturbation integration is assessed following the same method as the CMLM perturbation integrations. All five integrations used in this study are summarized in Table 2.

3. Results

a. CMLM-E Experiment

We will begin with the results from the CMLM-E experiment to describe the responses most directly driven by North Pacific OHFC anomalies. The annual cycles of the responses within the forcing region (35-45°N, 140-180°E) are presented in Fig. 2. Ocean temperatures increase throughout the water column as a direct response to the specified anomalous OHFC. Maximum temperature anomalies are found around 300 m, although the specified anomalous OHFC is largest near the surface (Fig. 1b). The maximum warming is located below the maximum winter MLD (~ 220 m) due to damping of the temperature anomalies within the mixed layer by the surface heat flux. Maximum SST anomalies are found in February and March due to the maximum anomalous OHFC forcing as well as the deepest mixed layer which entrains warmer anomalies from the thermocline. The mixed layer is deeper in the perturbation experiment (thick solid line in the bottom panel of Fig. 2) than the control integration (dashed line in the same panel) especially in winter by up to 100 m. Deepening of the winter mixed layer is primarily due to a weakening of the stratification in response to the specified anomalous OHFC between 100 and 200 m where the top of the thermocline is located in the control integration.

Net surface heat flux anomalies are from the ocean to atmosphere year-round, with maximum values in January-March (Fig. 2). The net surface heat flux feedback in December-March ranges from 26 to 33 W m^{-2} $°C^{-1}$, somewhat smaller than the corresponding values estimated from the observations (40-50 W m^{-2} $°C^{-1}$) (Frankignoul and Kestenare 2002; Park et al. 2005) and the CCSM2 (39 W m^{-2} $°C^{-1}$ for the December-March average) (Kwon and Deser 2007). The annual cycle of the atmospheric diabatic

heating response closely follows that of the net surface heat flux. The significant responses reach up to ~400 hPa from September to March. Diabatic heating responses near the surface below ~900 hPa are dominated by the vertical diffusion of sensible surface heat flux anomalies, while condensational heating anomalies are primarily responsible for the responses above ~900 hPa.

Hereafter, we focus on the January-March (winter) average response. The monthly responses during November-April are provided in Figs. S3 and S4 of the web supplement. A cross-section of the winter response along 40°N exhibits maximum MLD, surface heat flux, and diabatic heating anomalies near the western end of the section (Fig. 3), collocated with the maximum specified OHFC (Fig. 1). The cross-section exhibits a marked contrast between the directly forced region to the west of the dateline and the downstream region to the east of the dateline where the surface heat flux response is weak and negative, i.e. from atmosphere to ocean. The anomalous heat is transported from the forcing region by the mean westerlies and deposited into the ocean *via* surface heat flux anomalies to cause a warming downstream. In contrast to the subsurface temperature anomaly maximum in the directly forced region west of the dateline, positive ocean temperature anomalies east of the dateline are concentrated within the mixed layer, although vertical diffusion extends them downward. Similarly, the diabatic heating response exhibits a maximum in the middle troposphere near the forcing region, while to the east of the dateline it is confined near the surface and is due to vertical diffusion associated with anomalous sensible surface heat flux from atmosphere to ocean.

The spatial pattern of the winter SST response in the forcing region directly reflects that of the OHFC forcing (Fig. 4a). However, the amplitude of the SST response is about

four times larger than the root-mean-square of 10-year low-pass filtered SST in the same region (35-45°N, 140-180°E) from the CCSM2, i.e. 3.0°C for the CMLM-E compared to 0.7°C for the CCSM2. The discrepancy is large considering the OHFC forcing for this study is derived from the root-mean-square of 10-year low-pass filtered geostrophic OHFC from the CCSM2. Lack of dynamical damping due to lateral processes in the MLM, i.e. lateral advection as well as diffusion, appears to be responsible for the discrepancy. In CCSM2, the decadal SST anomalies are formed near the coast of Japan by the anomalous geostrophic OHFC, and then advected eastward along the Kuroshio Extension (*see* Fig. 3 of Kwon and Deser, 2007). The excessive SST anomalies are in turn responsible for the weaker surface heat flux feedback in CMLM-E than CCSM2.

Weak (< 1°C) positive SST anomalies outside of the forcing region are driven by atmosphere-to-ocean (i.e. negative) surface heat flux anomalies (Fig. 4a-b). The spatial pattern of the surface heat flux and the 850 hPa diabatic heating anomalies exhibit a clear distinction between the directly forced region in the Kuroshio Extension and the opposite-signed anomalies outside of this region. The spatial pattern of positive diabatic heating anomalies does not change much up to 400 hPa except for a slight eastward displacement with height (not shown). The surface wind stress response exhibits an anomalous cyclonic circulation basin-wide in extent and centered over the maximum positive SST anomalies along the Kuroshio Extension (Fig. 4d). The comparison with the climatological mean zonal wind stress (contours in the Fig. 4d) suggests that the anomalies represent a southward shift of the surface westerly jet. The anomalous cyclonic wind stress, i.e. positive wind stress curl anomalies, in response to warm SST anomalies

in the Kuroshio Extension is consistent with the results inferred from CCSM2 by Kwon and Deser (2007).

The CMLM-E sea-level pressure (SLP) and 250 hPa geopotential height (Z250) responses for January-March in the Northern Hemisphere north of 20°N are presented in the first column of Fig. 5 along with the SST and net surface heat flux responses. The basin-wide negative SLP anomalies in the North Pacific correspond to the cyclonic wind stress anomalies in Fig. 4d. The maximum low pressure anomaly is located slightly downstream of the maximum SST anomaly with amplitude ~ 2 hPa in response to a ~ 3°C SST warming averaged over the forcing region. A significant high pressure response is found over the North Atlantic and downstream over western Siberia, with maximum amplitude ~ 2 hPa. The Z250 responses exhibit generally positive anomalies over high latitudes, with a maximum over the North Atlantic (~40 m), and negative anomalies to the south. The zonally asymmetric component of the Z250 response exhibits a circumglobal zonal wavenumber five pattern along the midlatitude jet (Branstator 2002). The vertical structure of the circulation response is baroclinic over the north Pacific and equivalent barotropic over the North Atlantic and western Siberia. The North Atlantic component of the response is robust and stable throughout the winter months November-March, while the negative SLP anomaly response in the North Pacific begins to emerge in December and exhibits full amplitude from January through March, following the development of the SST anomalies (Fig. 6). The Z250 anomalies in the North Pacific remain positive throughout the winter although their location and magnitude vary substantially from month to month (see Fig. S3 in the web supplement).

b. CMLM-G Experiment

The CMLM-G exhibits very similar winter SST and surface heat flux responses to those of CMLM-E (Fig. 5). However, the SLP and the Z250 anomalies from the two experiments bear some interesting differences. Over the North Pacific, the negative (positive) SLP (Z250) response in CMLM-G is approximately half (double) the magnitude of that in CMLM-E. In addition, the response over the north Atlantic is diminished considerably and shifted eastward. To highlight the differences between the two experiments, the CMLM-G responses minus the corresponding CMLM-E responses are presented in the third column of Fig. 5. The differences in the atmospheric circulation responses consist of an equivalent barotropic ridge over the North Pacific and a more spatially-confined equivalent barotropic low over the North Atlantic, with maximum anomalies ~ 2 hPa in SLP and ~ 30 m in Z250. The Z250 difference pattern resembles the Pacific-North American (PNA) teleconnection pattern (Wallace and Gutzler 1981), although the downstream center over the subpolar North Atlantic is stronger than typical. The SST differences exhibit positive anomalies ~ 0.2°C directly south of the forcing region and a smaller patch of negative anomalies to the north. These weak SST anomalies appear to be driven by the anomalous circulation associated with the high SLP anomalies as indicated by the anomalous atmosphere-to-ocean heat flux. Anomalous atmosphere-to-ocean heat flux differences associated with the SLP differences also appear to drive the SST differences in the North Atlantic.

What drives the differences in the circulation responses in CMLM-E and CMLM-G, in particular the equivalent barotropic high over the North Pacific and associated PNA pattern? We argue that the presence of an interactive ocean mixed layer in the tropics in

CMLM-G leads to a tropical rainfall response which in turn provides an additional forcing mechanism for the extratropical atmospheric circulation. Fig. 7 shows that CMLM-E does not exhibit any significant tropical rainfall response while CMLM-G shows negative (positive) rainfall anomalies along the equator (~5°N) in the central and western tropical Pacific, with maximum amplitudes ~ ±1 mm day^{-1}, which corresponds to about 40 % of the root-mean-square of December-February average tropical precipitation in CCSM2. The CMLM-G rainfall anomalies are accompanied by weak but significant tropical SST anomalies (~ ±0.2°C; not shown). Note that the tropical rainfall anomalies are averaged over December-February to account for the approximately 1-month delay between tropical forcing and extra-tropical atmospheric circulation response (Trenberth et al., 1998; Alexander et al. 2002). The anomalous precipitation pattern in CMLM-G, which implies a northward migration of the Inter-Tropical Convergence Zone (ITCZ), resembles that of ENSO in its negative phase (Deser et al. 2006). Indeed, the ENSO regression patterns using variables from the CCSM2 control integration are generally consistent with the CMLM-G minus CMLM-E responses, although the amplitudes are about 50% greater (not shown).

c. AGCM-E

Next, we compare the CMLM approach with the traditional specified-SST approach for assessing the atmospheric response to anomalous SSTs. In AGCM-E, SST anomalies identical to those in CMLM-E are specified over the forcing region (35-45°N, 140-180°E; Fig. 5). The general features of the circulation responses in the two experiments are similar, with a baroclinic vertical structure over the North Pacific and an equivalent

barotropic structure over the North Atlantic and Siberia. However, the North Pacific SLP response is more spatially confined over the western half of the basin in AGCM-E compared to CMLM-E. Thus, the SLP anomalies averaged over the North Pacific basin (20-60°N, 140°E-120°W) are -0.83 hPa for CMLM-E compared to only -0.26 hPa for AGCM-E. The weaker January-March average response in AGCM-E is due to the rapid decay of the response in late winter, a feature not seen in CMLM-E (Fig. 6). By March, the amplitude of the SLP anomalies averaged over the North Pacific basin (20-60°N, 140°E-120°W) in AGCM-E is <10 % of that in CMLM-E and insignificant except for a small region east of Japan (Fig. 6). In addition to differences in the SLP responses, the Z250 response over the North Pacific (Atlantic) is larger (smaller) in AGCM-E compared to CMLM-E. Unlike the SLP response, the Z250 response in AGCM-E does not exhibit a weakening in late winter over the North Pacific (see Fig. S7 of the web supplement).

We propose that most of the differences between the AGCM-E and CMLM-E responses can be attributed to the role of the ocean mixed layer outside of the forcing region. In particular, AGCM-E exhibits a larger atmosphere-to-ocean heat flux to the east of the dateline compared to CMLM-E (and CMLM-G) along 40°N (see Fig. 8) because the fixed SST in AGCM-E acts as an infinite heat reservoir (Barsugli and Battisti 1998). The maximum atmosphere-to-ocean heat flux anomaly is -37 W m^{-2} in AGCM-E, while it is -12 W m^{-2} and -10 W m^{-2} in CMLM-E and CMLM-G, respectively. As a result, the associated negative diabatic heating anomalies east of the dateline in AGCM-E exhibit greater amplitude than either CMLM experiment. We conjecture that this anomalous diabatic cooling to the east of the dateline drives a local positive SLP response that acts to partially offset the negative SLP response due to the positive SST anomalies in the

Kuroshio Extension. Consequently, the atmospheric temperature and low-level geopotential height responses are more confined to the western portion of the basin in AGCM-E than CMLM-E (Fig. 8). In AGCM-E, the growth of the SST anomalies in the forcing region from December through March leads to a corresponding growth in the negative diabatic heating response to the east which in turn explains the progressive weakening of the negative SLP response as documented in Fig. 6. It is worth noting that AGCM-E exhibits insignificant tropical precipitation responses in all months (not shown).

d. Wind stress curl response

Part of the motivation for this study is to better understand the atmospheric circulation response to SST anomalies in the Kuroshio Extension region due to its crucial role in sustaining the decadal coupled atmosphere-ocean mode in CCSM2 (Kwon and Deser 2007). Of particular importance is the wind stress curl component of the response which drives geostrophic ocean circulation changes that in turn alter SSTs in the Kuroshio Extension region. The JFM wind stress curl responses in CMLM-E, CMLM-G and AGCM-E are shown in Fig. 9; their annual mean counterparts are given in Fig. S5 of the web supplement. The patterns of wind stress curl response are similar in all 3 experiments, with comparable amplitudes for CMLM-E and AGCM-E and weaker magnitudes for CMLM-G, in keeping with the SLP responses (recall Fig. 5). One may infer from the difference between the CMLM-G and CMLM-E wind stress curl responses that the tropically-forced teleconnection partially opposes the direct response (Figs. 9d and S5e). Thus, the thermally-coupled tropics act as a damping to the North Pacific decadal oscillation in CCSM2.

4. Discussion

a. Role of the tropical ocean mixed layer

The winter atmospheric circulation response to anomalous OHFC in the Kuroshio Extension is substantially modified by the presence of a thermodynamically active ocean mixed layer in the tropics. When the tropical ocean mixed layer is active, the Pacific ITCZ shifts northward toward the warmed hemisphere, consistent with previous studies (e.g. Chiang and Bitz 2005; Kang et al. 2008). The ITCZ displacement induces an extratropical PNA-like atmospheric response, with an equivalent barotropic ridge over the North Pacific that competes with the locally-forced baroclinic response especially in late winter (see Fig. S6 of the web supplement). The mechanism for the northward displacement of the Pacific ITCZ in our experiments with an active tropical ocean mixed layer requires further investigation. A possible explanation is the framework proposed by Kang et al. (2008) in which atmospheric meridional energy fluxes change to compensate the implied oceanic fluxes associated with the imposed OHFC anomaly. In addition, the wind-evaporation-SST feedback mechanism may also be important (Chiang and Bitz 2005).

b. Role of the extratropical ocean mixed layer

In late winter, the presence of an active ocean mixed layer in the extra-tropics leads to a stronger surface low response over the north Pacific compared to the case without an ocean mixed layer (recall Fig. 6). We propose that this is due not to any influence from the tropics, but because the 'specified-SST' experiment (AGCM-E) lacks the so-called

"reduced damping" effect due to thermal adjustment between ocean and atmosphere (Barsugli and Battisti, 1998). That is, excessive heat loss from the atmosphere to the ocean in the 'specified SST' experiment acts as a negative feedback to the direct response not just to the east of the dateline but also within the forcing region. This result suggests a potential deficiency inherent in specified-SST experiments. We note that in the case of perpetual experiments for a given month (e.g. Peng et al. 1997), the negative feedback could have ample time to grow and completely offset the primary response.

Liu and Wu (2004) also considered the lack of "reduced damping" when comparing their specified SST experiment with their fully coupled model and specified surface heat flux experiments. However, in contrast to our results, their specified SST and coupled model experiments yielded similar atmospheric circulation responses. We note, however, that Liu and Wu's findings are based on ensemble integrations for early winter (November-December) with constant amplitude SST forcing, in contrast to our results for late winter and amplifying SST anomalies.

c. Comparison with previous studies

As discussed in the Introduction, Yulaeva et al. (2001) conducted an experiment very similar to CMLM-G. However, unlike the baroclinic (low-level trough, upper-level ridge) response found in CMLM-G, Yulaeva et al. (2001) obtained an equivalent barotropic response consisting of a trough over and downstream of the forcing region directly east of Japan and a ridge over Alaska and western Canada. The possible role of tropical precipitation changes in modifying the atmospheric circulation response over the north Pacific was not explored in Yulaeva et al. (2001), although their experimental design

included an interactive ocean mixed layer in the tropics. This aspect, coupled with the relatively small sample size (10 ensemble members compared to ~ 100 here) and different definition of winter (December-February compared to JFM here), makes it difficult to ascertain the causes for the differing responses in Yulaeva et al. (2001) and CMLM-G. In terms of wind stress curl, the north Pacific response in Yulaeva et al. (2001) resembles that in CMLM-G (and CMLM-E), with positive anomalies in the latitude band 30°-50°N which in turn provides a negative feedback to the prescribed OHFC. Thus, their wind stress curl response would support the existence of a coupled atmosphere-ocean decadal oscillation as in our experiments, despite difference in the vertical structures of the atmospheric circulation response.

The fully coupled model experiments by Liu and Wu (2004) and Liu et al. (2007) may also have involved tropical precipitation anomalies but these were not explicitly examined. Liu et al. (2007) compared the responses for November-January and February-April and found an equivalent barotropic ridge response in early winter and a baroclinic (low-level trough and upper-level ridge) response in late winter. The monthly evolution of the atmospheric response in our coupled model experiments (CMLM-E and CMLM-G) is largely consistent with that of Liu et al. (2007), although the equivalent barotropic ridge response is confined to November with a gradual strengthening of the baroclinic response from December to March.

d. CCSM2 North Pacific decadal variability

Kwon and Deser (2007) empirically diagnosed the wind stress curl response to anomalous geostrophic OHFC along the Kuroshio Extension in CCSM2 by linearly

regressing the anomalous wind stress curl field lagged by 1-year upon the Kuroshio Extension SST anomaly index. The 1-yr lag was used to distinguish the atmospheric response to SST from the atmospheric forcing of SST which is otherwise confounded in the simultaneous regression. This approach relies on the fact that the wind stress curl anomalies contain practically no memory from one year to the next, while SST anomalies exhibit high persistence from one winter to the next. The CCSM2 JFM SLP and Z250 responses obtained using this empirical technique are shown in Fig. 10, scaled by the ratio of the standard deviation of the CCSM2 and CMLM-E SST anomalies averaged over the Kuroshio Extension (0.7ºC/3.0ºC; recall section 3a). The pattern of the SLP response in CCSM2 is similar to that in CMLM-E, with negative values over the North Pacific centered along 40ºN and weaker positive values north of 60ºN; however, the amplitudes are approximately twice as large. The Z250 response pattern in CCSM2 differs considerably from that in CMLM-E, with positive values over the subtropical Pacific, negative values over the North Pacific centered along 40ºN and positive values over northwestern Canada and eastern Siberia. Thus, the extra-tropical response is equivalent barotropic, even over the North Pacific, unlike that in CMLM-E, CMLM-G or AGCM-E. The tropical precipitation response in CCSM2 exhibits positive values along the equatorial Pacific in association with a southward shift of the ITCZ (Fig. 7d), which may in turn induce an equivalent barotropic deepening of the Aleutian Low.

The tropical precipitation responses in CCSM2 and CMLM-G are largely opposite (Fig. 7), suggesting that dynamical ocean processes contribute significantly to the tropical response in CCSM2. Chiang et al. (2008) also found that the inclusion of ocean dynamics yields a tropical response that is largely opposite to that induced by thermodynamic

ocean mixed layer processes (e.g., the WES feedback; Chiang and Bitz, 2005). A caveat to the CCSM2 results, however, is that the methodology used to define the atmospheric circulation response (e.g., 1-year lag regression) may alias the prominent biennial ENSO signal present in CCSM2 (Deser et al., 2006). Further experiments are needed to assess the role of dynamical ocean processes in the tropical SST and rainfall responses to anomalous OHFC in the Kuroshio Extension. We also note that the spatial patterns of the tropical rainfall responses in CMLM-G and CCSM2 are not identical. In CMLM-G, the rainfall anomalies are mainly concentrated within the northern ITCZ, while in CCSM2 they exhibit comparable amplitude along the equator and the ITCZ. These differences may reflect differences in their climatologies which show a more zonally oriented South Pacific Convergence Zone (SPCZ) and a stronger equatorial dry zone in the western Pacific in CCSM2 compared to CMLM-G.

Despite the fact that the north Pacific SLP response is more than twice as large in CCSM2 as in CMLM-E, the north Pacific wind stress curl response is only 1.2 times as large (Fig. 11). This is due to the fact that the anomalous wind stress curl is proportional to the amplitude of the anomalous SLP and inversely proportional to the spatial scale of the anomalous SLP *via* the Laplacian operator. The larger spatial scale of the SLP response in CCSM2 compared to CMLM-E partially offsets the difference in amplitude, yielding a more comparable wind stress curl response. A similar mismatch between the SLP and wind stress curl responses is found for CMLM-E *vs.* CMLM-G: the SLP (wind stress curl) response in CMLM-G is ~50% (80%) of that in CMLM-E. This mismatch occurs because the remote component of the North Pacific SLP response forced by tropical precipitation anomalies has a broader spatial scale than the local component of

the SLP response forced directly by the Kuroshio Extension SST anomalies. Thus, due to their larger spatial scale, tropical atmospheric teleconnections may have a smaller influence on wind stress curl than on SLP over the North Pacific, a result that has implications for decadal variability of the Pacific coupled atmosphere-ocean system.

5. Conclusion

The wintertime (JFM) response of the coupled atmosphere - ocean mixed layer system to geostrophic OHFC anomalies in the Kuroshio Extension has been examined by means of experiments with an AGCM coupled to an entraining ocean mixed layer model. In addition to the direct response, interaction with the tropics and the role of the extra-tropical ocean mixed layer were addressed through modifications of the experimental design.

The direct coupled ocean mixed layer - atmospheric circulation response to a positive OHFC anomaly in the Kuroshio Extension (experiment CMLM-E) consists of positive SST anomalies along the Kuroshio Extension and a baroclinic atmospheric response characterized by a low-level trough and upper-level ridge over the north Pacific. For an average SST anomaly of 3°C within the Kuroshio Extension region, the response amplitudes over the North Pacific are approximately 2 hPa for SLP and 10-20 m for Z250. In addition to the North Pacific response, an equivalent barotropic ridge response is found over the North Atlantic centered at 50°N, with amplitudes ~ 2 hPa for SLP and 40 m for Z250 hPa. These atmospheric circulation anomalies drive a weak (0.2-0.7°C) SST warming of the North Atlantic *via* perturbations to the surface turbulent energy flux.

When the ocean mixed layer is thermodynamically coupled to the atmosphere in the tropics as well as the extra-tropics (experiment CMLM-G), the tropical Pacific ITCZ shifts northward in response to oceanic warming along the Kuroshio Extension. The meridional displacement of the ITCZ generates a PNA-like atmospheric response that includes an equivalent barotropic ridge over the North Pacific. This tropically-induced teleconnection modifies the direct coupled atmospheric circulation response, reducing the surface trough and enhancing the upper level ridge over the North Pacific.

The uncoupled atmospheric circulation response to a positive SST anomaly along the Kuroshio Extension (experiment AGCM-E) is generally similar to the coupled response, except that the anomalous SLP trough over the north Pacific is confined to the western half of the basin in AGCM-E. This sensitivity of the north Pacific SLP response to the presence of an interactive ocean mixed layer was suggested to result from the artificial enhancement of the anomalous atmosphere-to-ocean net surface heat flux downstream of the Kuroshio Extension in AGCM-E (e.g., lack of reduced thermal damping) compared to CMLM-E. The atmospheric cooling that results from the net surface heat flux response drives a positive SLP anomaly that partially offsets the negative SLP anomaly that is a direct response to the warming along the Kuroshio Extension. This effect increases over time, such that by March the SLP trough response over the north Pacific is nearly absent in AGCM-E. This result may have implications for SST-forced AGCM experiments conducted in "perpetual mode" for which the month or season is kept fixed.

The AGCM, CMLM, and CCSM2 experiments are similar in terms of their wind stress curl responses despite differences in their SLP responses. This is due to that the tropically-induced portion of the SLP responses in CMLM-G and CCSM2 has a larger

spatial scale than the locally-induced SLP response, a factor which affects the wind stress curl *via* the Laplacian operator. This result has implications for decadal variability of the Pacific coupled ocean-atmosphere system to the extent that the north Pacific ocean gyre circulation is primarily driven by wind stress curl fluctuations.

Acknowledgments

We wish to acknowledge helpful discussions and technical support from many colleagues including D. Ferreira, J. Goodman, A. Phillips, and J. Yin. We gratefully acknowledge financial support from NOAA's Office of Global Programs (grant to C. Deser and Y.-O. Kwon).

References

Alexander, M. A., and C. Deser, 1995: A mechanism for the recurrence of wintertime midlatitude SST anomalies. *J. Phys. Oceanogr.*, **25**, 122-137.

Alexander, M. A., C. Deser, and M. S. Timlin, 1999: The re-emergence of SST anomalies in the North Pacific Ocean. *J. Climate*, **12**, 2419-2433.

Alexander, M. A., I. Blade, M. Newman, J. R. Lanzante, N.-C. Lau, and J. D. Scott, 2002: The atmospheric bridge: the influence of ENSO teleconnections on air-aea interaction over the global oceans. *J. Climate*, **15**, 2205-2231.

Barsugli, J. J., and D. S. Battisti, 1998: The basic effects of atmosphere-ocean thermal coupling on midlatitude variability. *J. Atmos. Sci.*, **55**, 477-493.

Berloff, P., A.M. Hogg, and W. Dewar, 2007: The turbulent oscillator: A mechanism of low-frequency variability of the wind-driven ocean gyres. *J. Phys. Oceanogr.*, **37**, 2363–2386.

Bonan, G. B., K. W. Oleson, M. Vertenstein, and S. Levis, 2002: The land surface climatology of the Community Land Model coupled to the NCAR Community Climate Model. *J. Climate*, **15**, 3123-3149.

Branstator, G., 2002: Circumglobal teleconnection, the jet stream waveguide, and the North Atlantic Oscillation. *J. Climate*, **15**, 1893-1910

Bretherton, C. S. and D. S. Battisti, 2000: An interpretation of the results from atmospheric general circulation models forced by the time history of the observed sea surface temperature distribution. *Geophys. Res. Lett.*, **27**, 767-770.

Briegleb, B. P., E. C. Hunke, C. M. Bitz, W. H. Lipscomb, M. M. Holland, J. L. Schramm, and R. E. Moritz, 2004: The sea ice simulation of the Community Climate System Model, version two. NCAR Tech. Note NCAR/TN-45 + STR, 34 pp.

Cassou, C., C. Deser, and M. A. Alexander, 2007: Investigating the impact of reemerging sea surface temperature anomalies on the winter atmospheric circulation over the North Atlantic. *J. Climate*, **20**, 3510-3526.

Cayan, D.R., 1992: Latent and Sensible Heat Flux Anomalies over the Northern Oceans: Driving the Sea Surface Temperature. *J. Phys. Oceanogr.*, **22**, 859–881.

Cessi, P., and F. Primeau, 2001: Dissipative selection of low-frequency modes in a reduced-gravity basin. *J. Phys. Oceanogr.*, **31**, 127–137.

Chang, E. K. M., S. Lee, and K. L. Swanson, 2002: Storm track dynamics. *J. Climate*, **15**, 2163-2183.

Chiang, J. C. H., and C. M. Bitz, 2005: Influence of high latitude ice cover on the marine Intertropical Convergence Zone. *Climate Dyn.*, **5**, 477-496, DOI: 10.1007/s00382-005-0040-5.

Chiang, J. C. H., W. Cheng, and C. M. Bitz, 2008: Fast teleconnections to the tropical Atlantic sector from Atlantic thermohaline adjustment. *Geophys. Res. Lett.*, submitted.

Deser and Timlin, 1997: Atmosphere–Ocean Interaction on Weekly Timescales in the North Atlantic and Pacific. *J. Climate*, **10**, 393–408.

Deser, C., A. Phillips, and J. W. Hurrell, 2004a: Pacific interdecadal climate variability: Linkages between the tropics and North Pacific during boreal winter since 1900. *J. Climate*, **17**, 3109-3124.

Deser, C., G. Magnusdottir, R. Saravanan, and A. Phillips, 2004b: The effects of North Atlantic SST and sea ice anomalies on the winter circulation in CCM3. Part II: Direct and indirect components of the response. *J. Climate*, **17**, 877–889.

Deser, C., A. Capotondi, R. Saravanan, and A. S. Phillips, 2006: Tropical Pacific and Atlantic climate variability in CCSM3. *J. Climate*, **19**, 2451-2481.

Deser, C., R. A. Tomas, and S. Peng, 2007: The transient atmospheric circulation response to North Atlantic SST and sea ice anomalies. *J. Climate*, **20**, 4751-4767.

Frankignoul, C., 1983: Sea surface temperature anomalies, planetary waves, and air-sea feedback in the middle latitudes. *Rev. Geophys*., **23**, 357-390.

Frankignoul, C., and E. Kestenare, 2002: The surface heat flux feedback. Part I: estimates from observations in the Atlantic and the North Pacific. *Climate Dyn.*, **19**, 633-647.

Frankignoul, C., P. Muller, and E. Zorita, 1997: A simple model of the decadal response of the ocean to stochastic wind forcing. *J. Phys. Oceanogr.*, **27**, 1533-1546.

Gaspar, P., 1988: Modeling the seasonal cycle of the upper ocean. *J. Phys. Oceanogr.*, **18**, 161-179.

Hendon, H. H., and D. L. Hartmann, 1982: Stationary waves on a sphere: Sensitivity to thermal feedback. *J. Atmos. Sci.*, **39**, 1906–1920.

Hoskins, B. J., and D. J. Karoly, 1981: The steady linear response of a spherical atmosphere to thermal and orographic forcing. *J. Atmos. Sci.*, **38**, 1179–1196.

Hurrell, J. W., 1995: Decadal trends in the North Atlantic Oscillation: regional temperatures and precipitation. *Science*, **269**, 676-679.

Kalnay et al., 1996: The NCEP/NCAR 40-year reanalysis project, *Bull. Amer. Meteor. Soc.*, **77**, 437-470.

Kang, S. M., I. M. Held, D. M. W. Frierson, M. Zhao, 2008: The response of the ITCZ to extratropical thermal forcing: idealized slab-ocean experiments with a GCM. *J. Climate*, **21**, 3521-3532.

Kelly, K. A., 2004: The relationship between oceanic heat transport and surface fluxes in the western North Pacific: 1970-2000. *J. Climate*, **17**, 573-588.

Kelly, K. A., and S. Dong, 2004: The relationship of western boundary current heat transport and storage to mid-latitude ocean-atmosphere interaction, in *Earth's Climate: The Ocean-Atmosphere Interaction*, edited by C. Wang, S.-P. Xie, and J. A. Carton, pp. 347-363, American Geophysical Union Geophysical Monograph 147.

Kiehl, J. T., and P. R. Gent, 2004: The community climate system model, version 2. *J. Climate*, **17**, 3666-3682.

Kumar, A., and M. P. Hoeling, 1998: Specification of regional sea surface temperature in atmospheric general circulation model simulations. *J. Geophys. Res.*, **103**(D8), 8901-8907.

Kushnir, Y., W. A. Robinson, I. Blade, N. M. J. Hall, S. Peng, and R. Sutton, 2002: Atmospheric GCM response to extratropical SST anomalies: Synthesis and evaluation. *J. Climate*, **15**, 2233-2256.

Kwon, Y.-O., and C. Deser, 2007: North Pacific decadal variability in the Community Climate System Model version 2. *J. Climate*, **20**, 2416-2433.

Latif, M., and T. P. Barnett, 1996: Decadal climate variability over the North Pacific and North America: Dynamics and predictability. *J. Climate*, **9**, 2407-2423.

Liu, Z., and L. Wu, 2004: Atmospheric response to North Pacific SST: The role of ocean-atmosphere coupling, *J. Climate*, **17**, 1859-1882.

Liu, Z., Y. Liu, L. Wu, and R. Jacob, 2007: Seasonal and long-term atmospheric responses to reemerging North Pacific Ocean variability: A combined dynamical and statistical assessment. *J. Climate*, **20**, 955-980.

Mantua, N. J., S. R. Hare, Y. Zhang, J. M. Wallace, and R. C. Francis, 1997: A Pacific interdecadal climate oscillation with impacts on salmon production. *Bull. Amer. Meteor. Soc.*, **78**, 1069-1079.

Marshall, J., H. Johnson, and J. Goodman, 2001: A study of the interaction of the North Atlantic Oscillation with ocean circulation. *J. Climate*, **14**, 1399-1421.

Neelin, J. D., and W. J. Weng, 1999: Analytical prototypes for ocean atmosphere interaction at midlatitudes. Part I: Coupled feedbacks as a sea surface temperature dependent stochastic process. *J. Climate*, **12**, 697-721.

Newman, M., G. P. Compo, and M. A. Alexander, 2003: ENSO-forced variability of the Pacific Decadal Oscillation. *J. Climate*, **16**, 3853-3857.

Park, S., C. Deser, and M. A. Alexander, 2005: Estimation of the surface heat flux response to sea surface temperature anomalies over the global oceans. *J. Climate*, **18**, 4582-4599.

Peng, S., and J. S. Whitaker, 1999: Mechanisms determining the atmospheric response to midlatitude SST anomalies. *J. Climate*, **12**, 1393-1408.

Peng, S., and W. A. Robinson, 2001: Relationships between atmospheric internal variability and the responses to an extratropical SST anomaly. *J. Climate*, **14**, 2943–2959.

Peng, S., W. A. Robinson, and M. P. Hoerling, 1997: The modeled atmospheric response to midlatitude SST anomalies and its dependence on background circulation states. *J. Climate*, **10**, 971-987.

Pierce, D. W., T. P. Barnett, N. Schneider, R. Saravanan, D. Dommenget, and M. Latif, 2001: The role of ocean dynamics in producing decadal climate variability in the North Pacific. *Climate Dyn.*, **18**, 51-70.

Qiu, B., 2000: Interannual variability of the Kuroshio Extension system and its impact on the wintertime SST field. *J. Phys. Oceanogr.*, **30**, 1486-1502.

Qiu, B., 2003: Kuroshio Extension variability and forcing of the Pacific decadal oscillations: Responses and potential feedback. *J. Phys. Oceanogr.*, **33**, 2465-2482.

Qiu, B., N. Schneider, and S. Chen, 2007: Coupled decadal variability in the North Pacific: An observationally constrained idealized model. *J. Climate*, **20**, 3602–3620.

Saravanan, R., and J. C. McWilliams, 1998: Advective ocean-atmosphere interaction: An analytical stochastic model with implications for decadal variability. *J. Climate*, **11**, 165-188.

Schneider, N., and B. D. Cornuelle, 2005: The forcing of the Pacific Decadal Oscillation. *J. Climate*, **18**, 4355-4373.

Schneider, N., A. J. Miller, and D. W. Pierce, 2002: Anatomy of North Pacific decadal variability. *J. Climate*, **15**, 586-605.

Seager, R., Y. Kushnir, N. H. Naik, M. A. Cane, and J. Miller, 2001: Wind-driven shifts in the latitude of the Kuroshio-Oyashio Extension and Generation of SST anomalies on decadal timescales. *J. Climate*, **14**, 4249-4265.

Smith, T. M., and R. W. Reynolds, 2003: Extended reconstruction of global sea surface temperature based on COADS data (1854-1997). *J. Climate*, **16**, 1495-1510.

Sutton, R., and P. P. Mathieu, 2002: Response of the atmosphere-ocean mixed layer system to anomalous ocean heat flux convergence. *Quart. J. Roy. Meteor. Soc.*, **128**, 1259-1275.

Tanimoto, Y., H. Nakamura, T. Kagimoto, and S. Yamane, 2003: An active role of extratropical sea surface temperature anomalies in determining anomalous turbulent heat flux. *J. Geophys. Res.*, **108**(C10), 3304, doi:10.1029/2002JC001750.

Thompson, D. W. J., and J. M. Wallace, 1998: The Arctic Oscillation signature in the wintertime geopotential height and temperature fields. *Geophys. Res. Lett.*, **25**, 1297-1300.

Trenberth, K. E., and J. M. Caron, 2001: Estimates of meridional atmosphere and ocean heat transports. *J. Climate*, **14**, 3433-3443.

Trenberth, K. E., G. W. Branstator, D. Karoly, A. Kumar, N.-C. Lau, and C. Ropelewski, 1998: Progress during TOGA in understanding and modelling global teleconnections associated with tropical sea surface temperatures. *J. Geophys. Res.*, **103(**C7), 14,291-14,324.

Vivier, F., K. A. Kelly, L. Thompson, 2002: Heat budget in the Kuroshio Extension region: 1993-1999, *J. Phys. Oceanogr.*, **32**, 3436-3454.

Wallace, J. M., and D. S. Grutzler, 1981: Teleconnections in the Geopotential Height Field during the Northern Hemisphere Winter, *Mon. Wea. Rev.*, **109**, 784-812.

Wunsch, C., 2005: The total meridional heat flux and its oceanic and atmospheric partition. *J. Climate*, **18**, 4374-4380.

Yulaeva, E., N. Schneider, D. W. Pierce, and T. P. Barnett, 2001: Modeling of North Pacific climate variability forced by oceanic heat flux anomalies. *J. Climate*, **14**, 4027-4046.

Table 1. Characteristics of the winter atmospheric circulation response to upper ocean thermal anomalies in the Kuroshio Extension region in various studies, except Sutton and Mathieu (2002) which is for the North Atlantic Gulf Stream Extension. Values in (not in) parentheses are not (are) statistically significant at the 95 % level; values within brackets lack estimates of statistical significance. Acronyms used are as follows: AGCM = Atmospheric General Circulation Model, OMLM = Ocean Mixed Layer Model, CGCM = Coupled Atmophere-Ocean General Circulation Model, ML = Mixed Layer, OHFC = Ocean Heat Flux Convergence, HFLX = Surface Heat Flux, T = Ocean Temperature, BC = Baroclinic, and BT = Equivalent Barotropic.

Reference	Experiment Type	Specified Anomalies	Month(s)	Maximum SST anomalies	Maximum Responses in the North Pacific					Active Tropics	Independent Sample Size
					SLP (hPa)	Z850 (m)	Z500 (m)	Z250 (m)	Overall		
Peng et al. (1997)	AGCM	SST	Perpetual Jan	2.5°C	-2.5	-12	-5	(0)	BC	No	384
			Perpetual Feb	2.5°C	(-0.6)	(+6)	+20	+30	BT Ridge	No	384
Yulaeva et al. (2001)	AGCM-OMLM	ML OHFC	DJF	0.75°C	-2	[-10]	-20	[-20]	BT Trough	Yes	10
Liu and Wu (2004)	AGCM	SST	Dec	2.0°C	+2	+20	+35	+40	BT Ridge	No	40
	AGCM	HFLX	Dec	0.4°C	-	-20	-	-40	BT Trough	No	40
	CGCM	0-200m T	Dec	1.6°C	+2.5	+20	+35	+40	BT Ridge	Yes	60
	CGCM	0-200m T	Dec	1.6°C	+5	+40	+65	+80	BT Ridge	Yes	40
Liu et al. (2007)	CGCM	0-560m T	NDJ	1.2°C	+1.5	+15	+15	+30	BT Ridge	Yes	160
			FMA	1.2°C	-0.5	-3	(0)	(+1)	BC	Yes	160
This Study	AGCM-OMLM	0-1000m OHFC	JFM	4.0°C	-2	-10	(+10)	+20	BC	No	100
	AGCM-OMLM	0-1000m OHFC	JFM	4.0°C	-1	(+10)	+20	+40	BC*	Yes	100
	AGCM	SST	JFM	4.0°C	-2	(+0)	(+10)	+30	BC	No	100
Sutton and Mathieu (2002)	AGCM-OMLM	ML OHFC	JFM	0.8°C	-5	-35	-60	-60	BT Trough	Yes	10

Table 2. Summary of the simulations used in this study. KE and OHFCA refer to the Kuroshio Extension (35-45°N, 140-180°E) and the ocean heat flux convergence anomalies, respectively.

Experiment Name	Specified Perturbation	Mixed Layer Ocean	Length of Integration
CMLM –C	None	Global	150 yr
CMLM-E	OHFCA within KE from CCSM2	Poleward of 20°N,S	100 yr
CMLM-G	OHFCA within KE from CCSM2	Global	100 yr
AGCM-C	None	None	150 yr
AGCM-E	SSTA within KE from CMLM-E	None	100 yr

Figure Captions

Figure 1. Decadal geostrophic ocean heat flux convergence anomalies for the CMLM perturbation integrations. (a) Map of March values integrated over upper 10 m. Contour interval is 2.5 W m^{-2}. (b) Values averaged over the Kuroshio Extension region (35-45°N, 140-180°E) as a function of month and depth, expressed as a temperature tendency (°C s^{-1}). Contour interval is 2×10^{-8}°C s^{-1}. Dashed line indicates the climatological monthly mean mixed layer depth (MLD) from the CCSM2 control integration. (c) Vertical section of March values along 40°N. Contour interval is 5×10^{-8}°C s^{-1} and 1×10^{-8}°C s^{-1}, for the thick and thin solid contours, respectively. Dashed line indicates the March climatological mean MLD from the CCSM2 control integration. (d) Same as (c), but along 150°E.

Figure 2. Annual cycle of CMLM-E responses averaged over the Kuroshio Extension (35-45°N, 140-180°E). (a) Diabatic heating. Contour interval is 2×10^{-6} K s^{-1}. Zero contour is suppressed. Shading indicates significance at 95 % level. (b) Net surface heat flux. Positive is from ocean to atmosphere. Note that the values for all 12 months are significant at 95 % level. (c) Ocean temperature. Contour interval is 0.5°C. Shading covers the whole section because all values are significant at 95 % level. Dashed thick contour is the MLD from the control integration and the solid thick contour is the MLD from the perturbation experiment. MLD anomalies for all the months except July are significant at 95 % level.

Figure 3. Same as Fig. 2 but for winter (JFM) CMLM-E responses along a zonal section averaged over 35-45°N. The contour interval is 5 × 10^{-6} K s^{-1} in (a) and 1°C starting from 0.5°C in (c). The net surface heat flux responses in (b) are significant at 95 % level except for the longitude band 195-205°E, and the MLD responses in (c) are significant at 95 % level except east of 215°E.

Figure 4. Winter (JFM) CMLM-E responses. (a) SST. Contour interval is 1°C, with the 0.25°C and 0.5°C contours indicated by the dashed lines. Shading indicates significance at 95 % level. (b) Net surface heat flux. Positive values denote a flux from ocean to atmosphere. Contour interval is 50 W m^{-2} for values greater than or equal to zero (solid contours); dashed contours show the -8 W m^{-2} values. (c) 850 hPa diabatic heating. Contour interval is 10 × 10^{-6} K s^{-1}. Dashed contours indicate -2 × 10^{-6} K s^{-1}. (d) Surface wind stress (vectors) superimposed upon zonal wind stress from the control integration (CMLM-C; contours). Contour interval is 0.05 N m^{-2}. Positive and zero (negative) values are plotted with solid (dashed) contours.

Figure 5. Winter (JFM) responses. (*Top row*) 250 hPa geopotential height, (*second row*) sea-level pressure, (*third row*) net surface heat flux, and (*bottom row*) SST from (*first column*) CMLM-E, (*second column*) CMLM-G, (*third column*) CMLM-G minus CMLM-E, and (*fourth column*) AGCM-E. Positive (negative) responses are plotted with solid (dashed) contours. Zero contours are suppressed. Contour intervals are 10 m, 1 hPa, 50 W m^{-2}, and 1°C, respectively. Note that the additional thin solid and dashed contours for the net surface heat flux and SST indicate ±10 W m^{-2} and ±0.2°C, respectively.

Shading indicates significance at 95 % level. The projection is for the northern hemisphere poleward of 20°N with the latitude circles at 40, 60 and 80°N.

Figure 6. Monthly equilibrium responses of (*top*) CMLM-E sea-level pressure, (*middle*) AGCM-E sea-level pressure, and (*bottom*) AGCM-E SST. Positive (negative) responses are plotted with solid (dashed) contours. Zero contours are suppressed. Contour intervals are 1 hPa. Shading indicates significance at 95 % level.

Figure 7. DJF responses of precipitation in the tropics for (a) CMLM-E, (b) CMLM-G, (c) CMLM-G minus CMLM-E, and (d) CCSM2. Note that the CCSM2 response is scaled by the ratio between the standard deviation of CCSM2 and CMLM-E SST anomalies averaged in the Kuroshio Extension. Positive (negative) responses are plotted with red (blue) contours. Zero contours are suppressed. Contour intervals are 0.5 mm day^{-1} for (a-c) and 1 mm day^{-1} for (d). Gray shading in (a-b) indicates significance at 95 % level, while the greenish shadings in (c-d) are the DJF mean precipitation from CMLM-E and CCSM2, respectively.

Figure 8. JFM equilibrium responses along a zonal section averaged for 30-50°N of (*top row*) geopontential height, (*second row*) atmospheric temperature, (*third row*) diabatic heating, and (*bottom row*) net surface heat flux from (*left*) CMLM-E, (*center*) CMLM-G, and (*right*) AGCM-E. (*Top three rows*) Positive (negative) responses are plotted with black (gray) contours. Zero contours are suppressed. Contour intervals are 5 m, 0.5 K, and 5×10^{-6} K s^{-1}, respectively. Shading indicates significance at 95 % level. (*Bottom*

row) Positive values indicate the anomalous net surface heat flux is from ocean to atmosphere. Dotted values are significant at the 95 % confidence level.

Figure 9. JFM wind stress curl responses from (a) CMLM-E, (b) CMLM-G, (c) AGCM-E, and (d) CMLM-G minus CMLM-E. Contour intervals are 2×10^{-8} N m^{-3}. Negative values are dashed and shading indicates significance at 95 % level.

Figure 10. JFM CCSM2 responses to the Kuroshio Extension SST anomalies for (a) 250 hPa geopotential height, and (b) sea-level pressure. The responses are scaled by the ratio between the standard deviation of CCSM2 and CMLM-E SST anomalies averaged in the Kuroshio Extension. Positive (negative) responses are plotted with solid (dashed) contours. Zero contours are suppressed. Contour intervals are 10 m and 1 hPa, respectively. Shading indicates significance at 95 % level.

Figure 11. JFM responses for (*top row*) sea-level pressure, (*middle row*) wind stress curl, and (*bottom row*) Laplacian of sea-level pressure from (*left column*) CMLM-E, (*center column*) CMLM-G, and (*right column*) CCSM2. The CCSM2 responses are scaled by the ratio between the standard deviation of CCSM2 and CMLM-E SST anomalies averaged in the Kuroshio Extension. Positive (negative) responses are plotted with solid (dashed) contours. Zero contours are suppressed in the sea-level pressure plots. Contour intervals are 1 hPa, 2×10^{-8} N m^{-3}, and 1.5×10^{-12} hPa m^2, respectively.

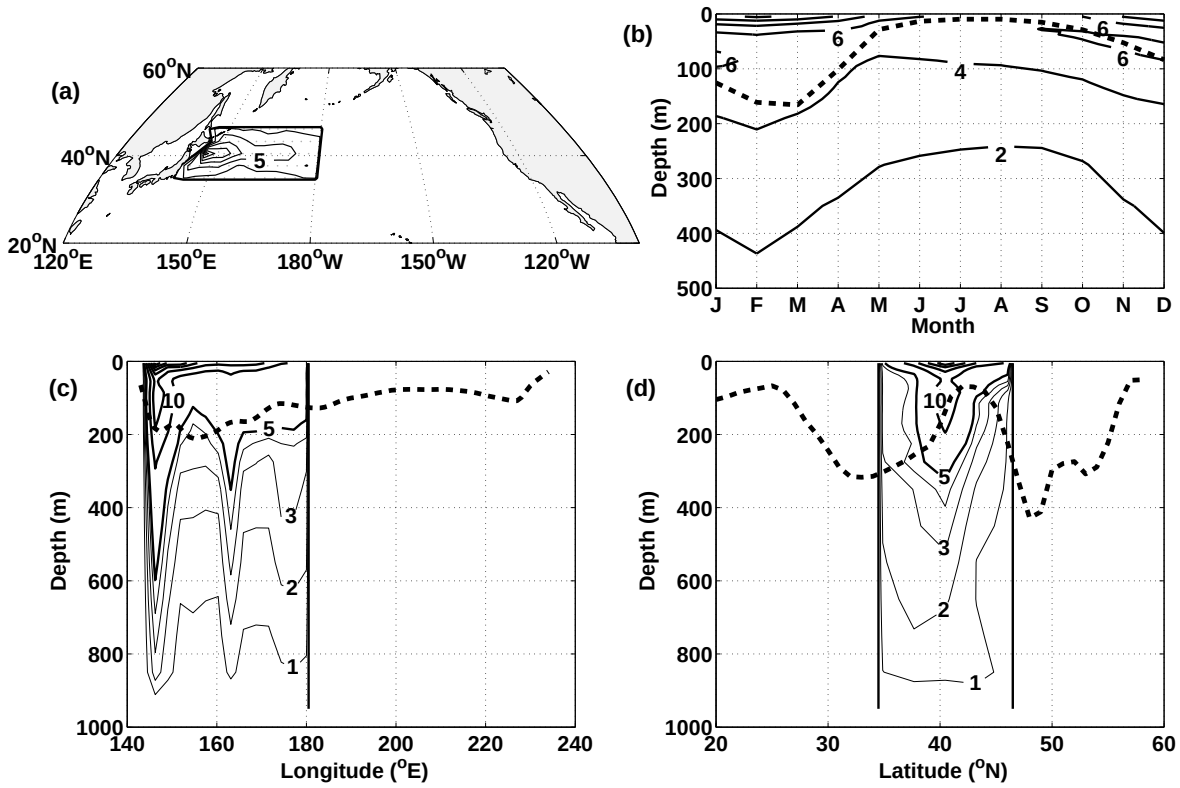

Figure 1: Decadal geostrophic ocean heat flux convergence anomalies for the CMLM perturbation integrations. (a) Map of March values integrated over upper 10 m. Contour interval is 2.5 W m^{-2}. (b) Values averaged over the Kuroshio Extension region (35-45^{o}N, 140-180^{o}E) as a function of month and depth, expressed as a temperature tendency (^{o}C s^{-1}). Contour interval is 2×10^{-8o}C s^{-1}. Dashed line indicates the climatological monthly mean mixed layer depth (MLD) from the CCSM2 control integration. (c) Vertical section of March values along 40^{o}N. Contour interval is 5×10^{-8o}C s^{-1} and 1×10^{-8o}C s^{-1}, for the thick and thin solid contours, respectively. Dashed line indicates the March climatological mean MLD from the CCSM2 control integration. (d) Same as (c), but along 150^{o}E.

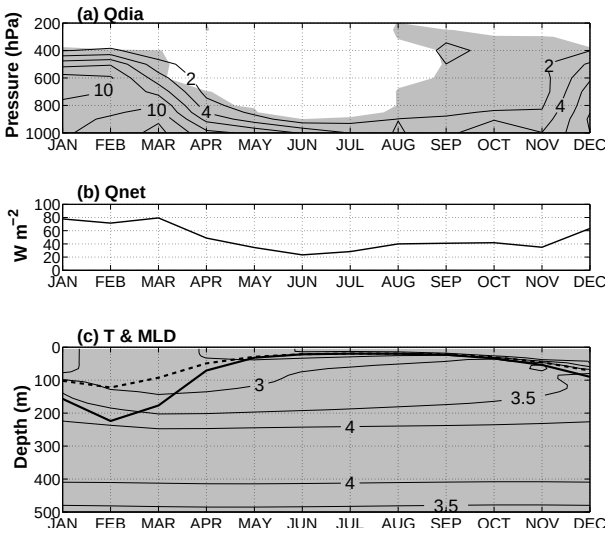

Figure 2: Annual cycle of CMLM-E response averaged over the Kuroshio Extension (35-45^{o}N, 140-180^{o}E). (a) Diabatic heating. Contour interval is 2×10^{-6} K s^{-1}. Zero contour is suppressed. Shading indicates significance at 95 % level. (b) Net surface heat flux. Positive is from ocean to atmosphere. Note that the values for all 12 months are significant at 95 % level. (c) Ocean temperature. Contour interval is 0.5^{o}C. Shading covers the whole section because all the values are significant at 95 % level. Dashed thick contour is the MLD from the control integration and the solid thick contour is the MLD from the pertubation experiment. MLD anomalies for all the months except July are significant at 95 % level.

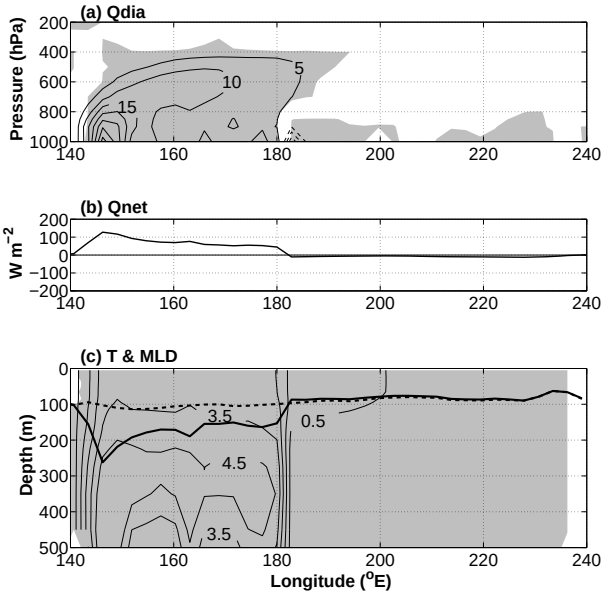

Figure 3: Same as Fig.2 but for winter (JFM) CMLM-E responses along a zonal section averaged for 35-45^{o}N. Note that the contour intervals are 5×10^{-6} K s^{-1} and 1^{o}C starting from 0.5^{o}C for the top and the bottom panel, respectively. Same as Fig. 2 but for winter (JFM) CMLM-E responses along a zonal section averaged over 35-45^{o}N. The contour interval is 5×10^6 K s^{-1} in (a) and 1^{o}C starting from 0.5^{o}C in (c). The net surface heat flux responses in (b) are significant at 95 % level except for the longitude band 195-205^{o}E, and the MLD responses in (c) are significant at 95 % level except east of 215^{o}E.

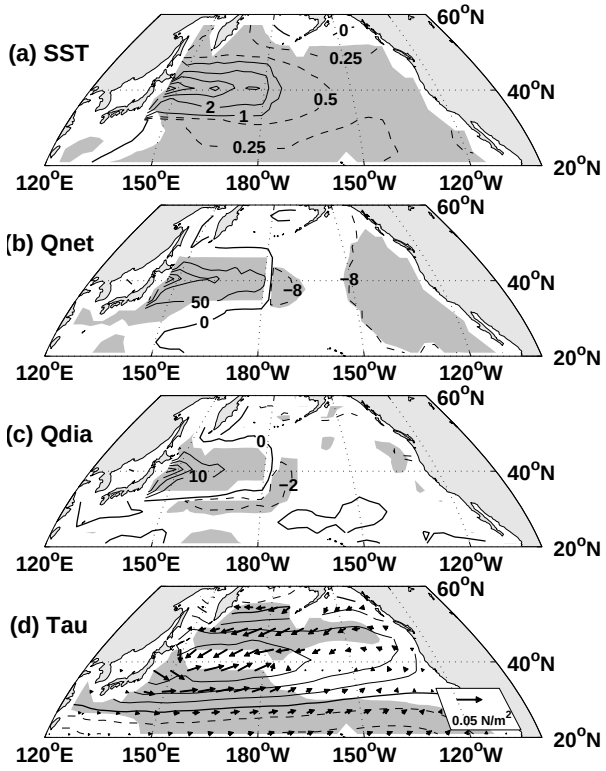

Figure 4: Winter (JFM) CMLM-E responses. (a) SST. Contour interval is 1^{o}C, with the 0.25^{o}C and 0.5^{o}C contours indicated by the dashed lines. Shading indicates significance at 95 % level. (b) Net surface heat flux. Positive values denote a flux from ocean to atmosphere. Contour interval is 50 W m^{-2} for values greater than or equal to zero (solid contours); dashed contours show the -8 W m^{-2} values. (c) 850 hPa diabatic heating. Contour interval is 10 $\times$ 10^{-6} K s^{-1}. Dashed contours indicate -2 $\times$ 10^{-6} K s^{-1}. (d) Surface wind stress (vectors) superimposed upon zonal wind stress from the control integration (CMLM-C; contours). Contour interval is 0.05 N m^{-2}. Positive and zero (negative) values are plotted with solid (dashed) contours.

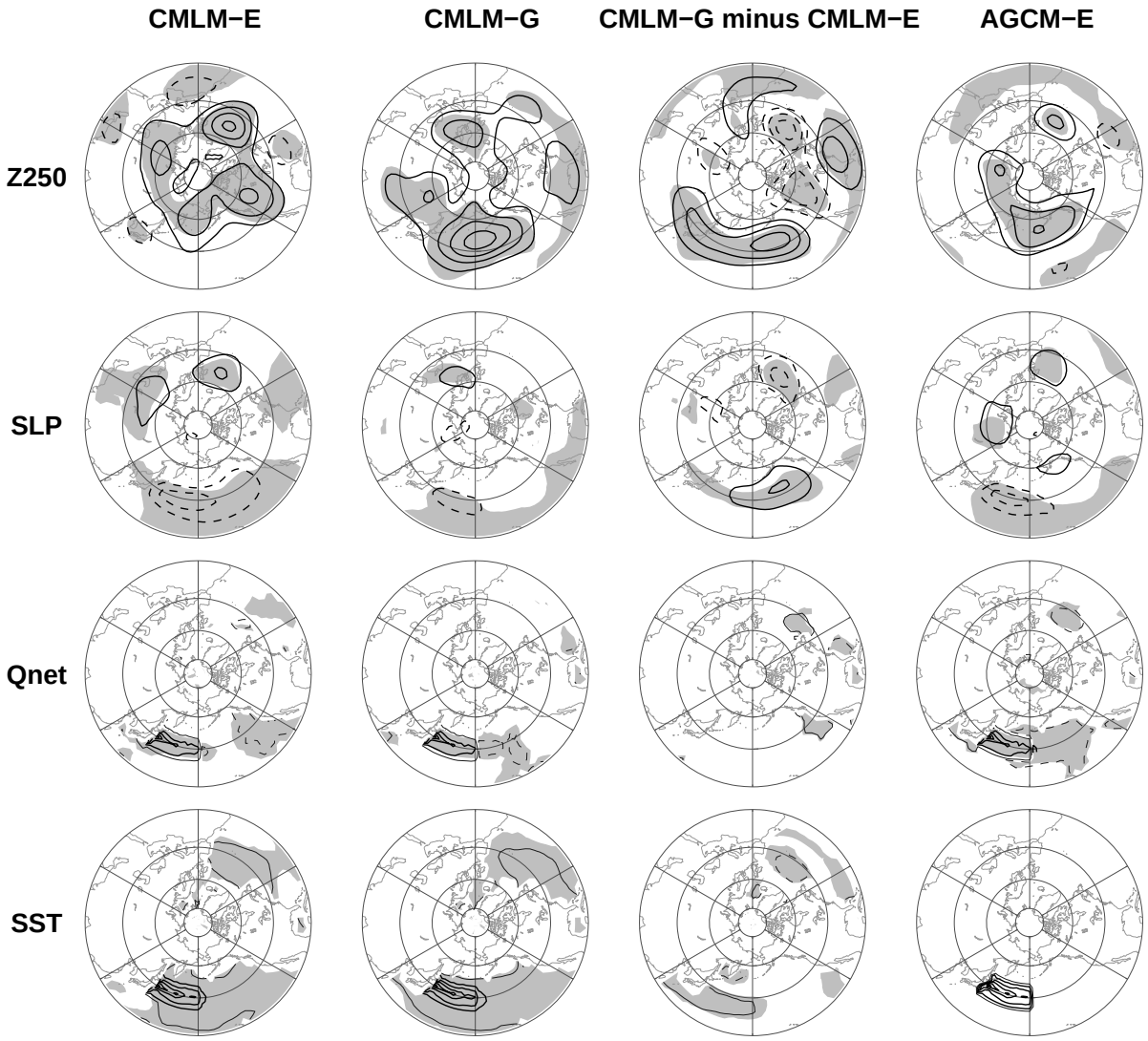

Figure 5: Winter (JFM) responses. (*Top row*) 250 hPa geopotential height, (*second row*) sea-level pressure, (*third row*) net surface heat flux, and (*bottom row*) SST from (*first column*) CMLM-E, (*second column*) CMLM-G, (*third column*) CMLM-G minus CMLM-E, and (*fourth column*) AGCM-E. Positive (negative) responses are plotted with solid (dashed) contours. Zero contours are suppressed. Contour intervals are 10 m, 1 hPa, 50 W m^{-2}, and 1^oC, respectively. Note that the additional thin solid and dashed contours for the net surface heat flux and SST indicate ± 10 W m^{-2} and $\pm 0.2^oC$, respectively. Shading indicates significance at 95 % level. The projection is for the northern hemisphere poleward of 20^oN with the latitude circles at 40, 60 and 80^oN.

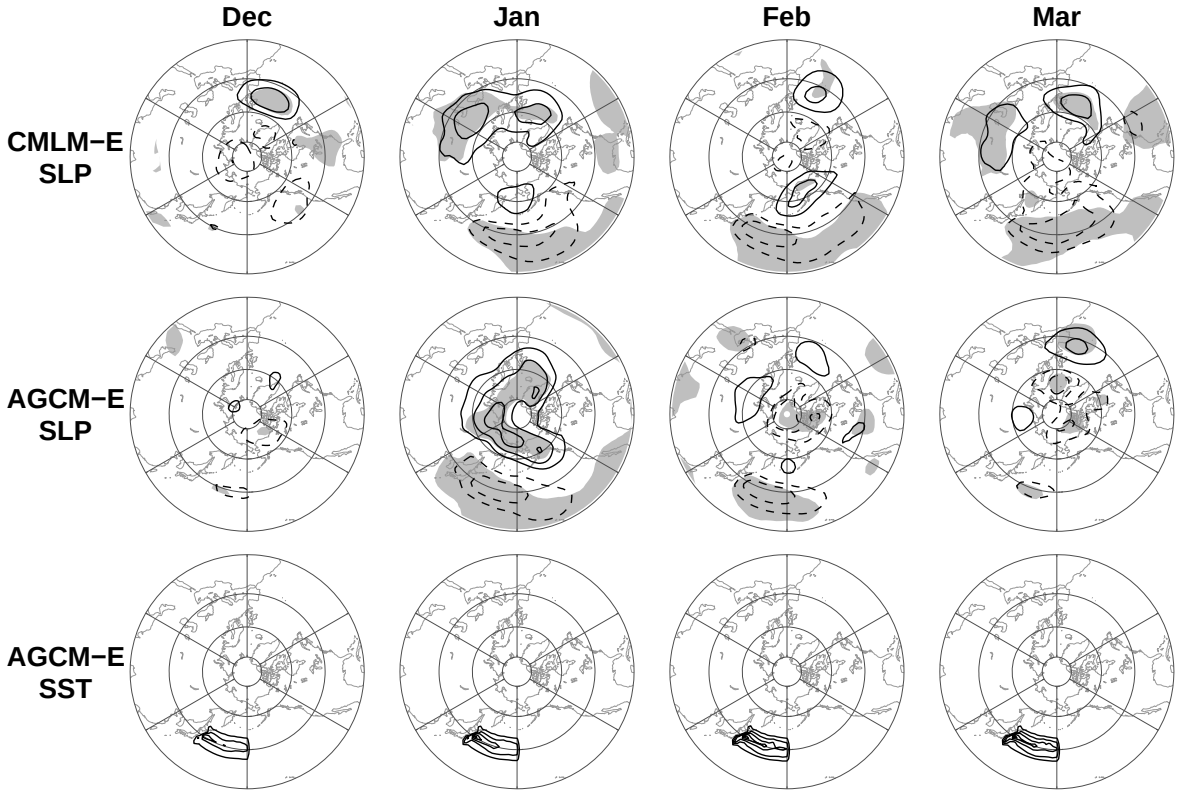

Figure 6: Monthly equilibrium responses of (*top*) CMLM-E sea-level pressure, (*middle*) AGCM-E sea-level pressure and (*bottom*) AGCM-E SST. Positive (negative) responses are plotted with solid (dashed) contours. Zero contours are suppressed. Contour intervals are 1 hPa and 1^oC, respectively. Shading indicates significance at 95 % level. The projection is for the northern hemisphere poleward of 20^oN with the latitude circles at 40, 60 and 80^oN.

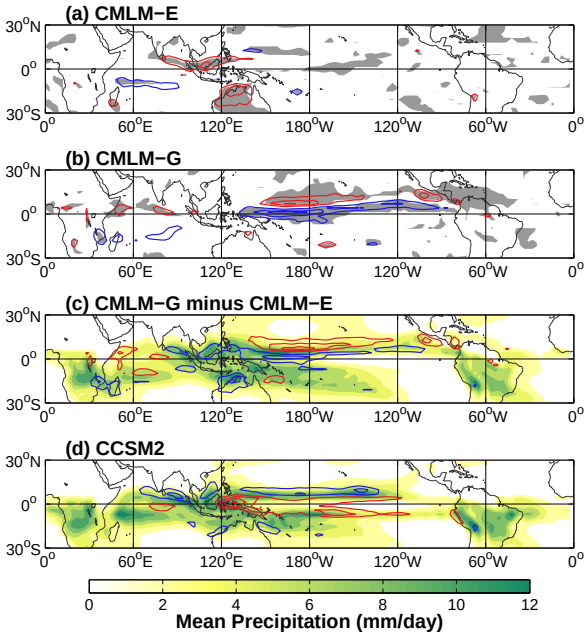

Figure 7: DJF responses of precipitation in the tropics for (a) CMLM-E, (b) CMLM-G, (c) CMLM-G minus CMLM-E, and (d) CCSM2. Note that the CCSM2 response is scaled by the ratio between the standard deviation of CCSM2 and CMLM-E SST anomalies averaged in the Kuroshio Extension. Positive (negative) responses are plotted with red (blue) contours. Zero contours are suppressed. Contour intervals are 0.5 mm day^{-1} for (a-c) and 1 mm day^{-1} for (d). Gray shadings in (a-b) indicates significance at 95 % level, while the greenish shadings in (c-d) are the DJF mean precipitation from CMLM-E and CCSM2, respectively.

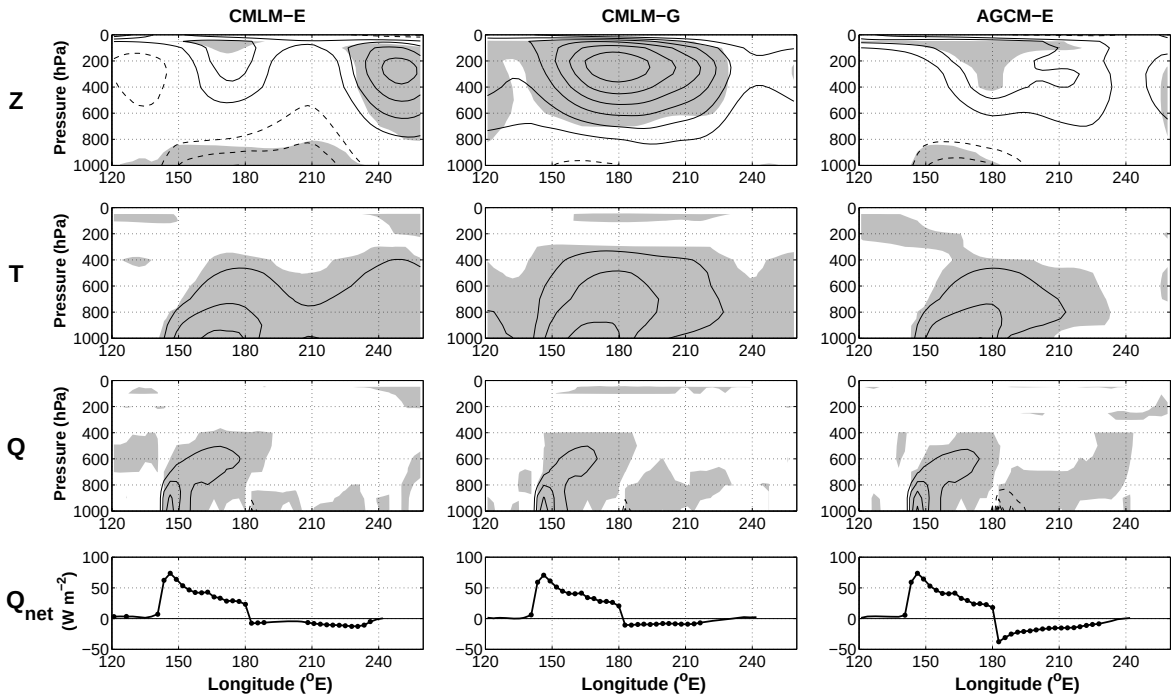

Figure 8: JFM equilibrium responses along a zonal section averaged for 30-50^{o}N of (*top row*) geopontential height, (*second row*) atmospheric temperature, (*third row*) diabatic heating, and (*bottom row*) net surface heat flux from (*left*) CMLM-E, (*center*) CMLM-G, and (*right*) AGCM-E. (*Top three rows*) Positive (negative) responses are plotted with solid (dashed) contours. Zero contours are suppressed. Contour intervals are 5 m, 0.5 K, and 5 $\times$ 10^{-6} K s^{-1}, respectively. Shading indicates significance at 95 % level. (*Bottom row*) Positive values indicate the anomalous net surface heat flux is from ocean to atmosphere. Dotted values are significant at the 95 % confidence level.

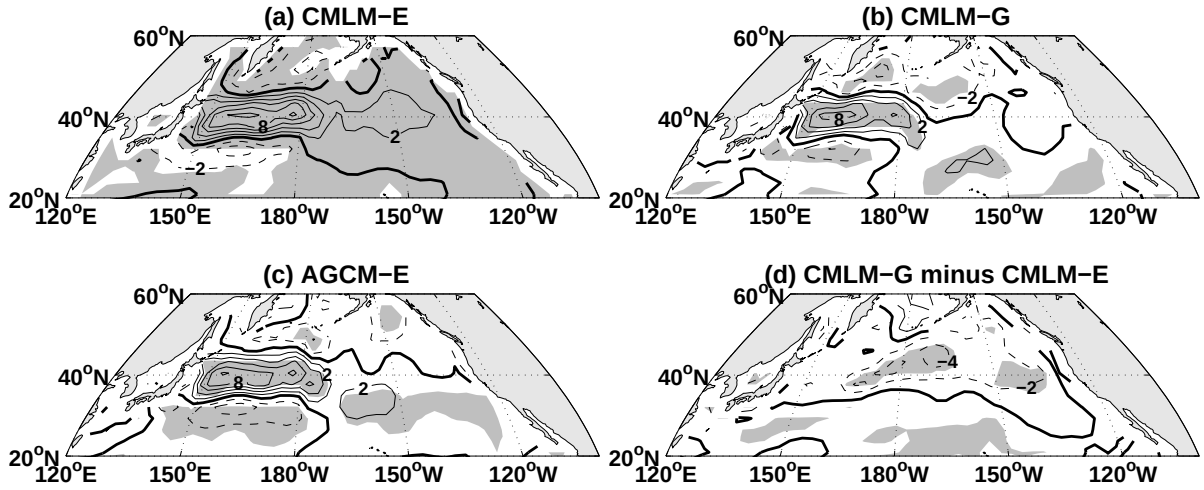

Figure 9: JFM wind stress curl responses from (a) CMLM-E, (b) CMLM-G, (c) AGCM-E, and (d) CMLM-G minus CMLM-E. Contour intervals are 2×10^{-8} N m^{-3}. Negative values are dashed and shading indicates significance at 95 % level.

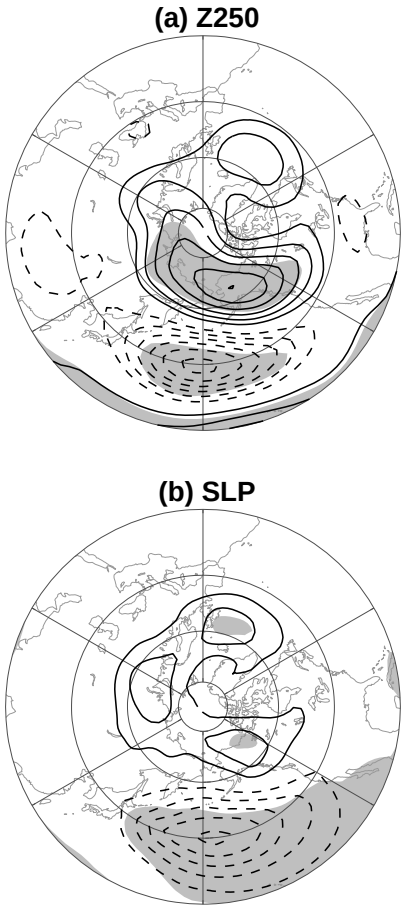

Figure 10: JFM CCSM2 responses to the Kuroshio Extension SST anomalies for (a) 250 hPa geopotential height and (b) sea-level pressure. The responses are scaled by the ratio between the standard deviation of CCSM2 and CMLM-E SST anomalies averaged in the Kuroshio Extension. Positive (negative) responses are plotted with solid (dashed) contours. Zero contours are suppressed. Contour intervals are 10 m and 1 hPa, and, respectively. Shading indicates significance at 95 % level.

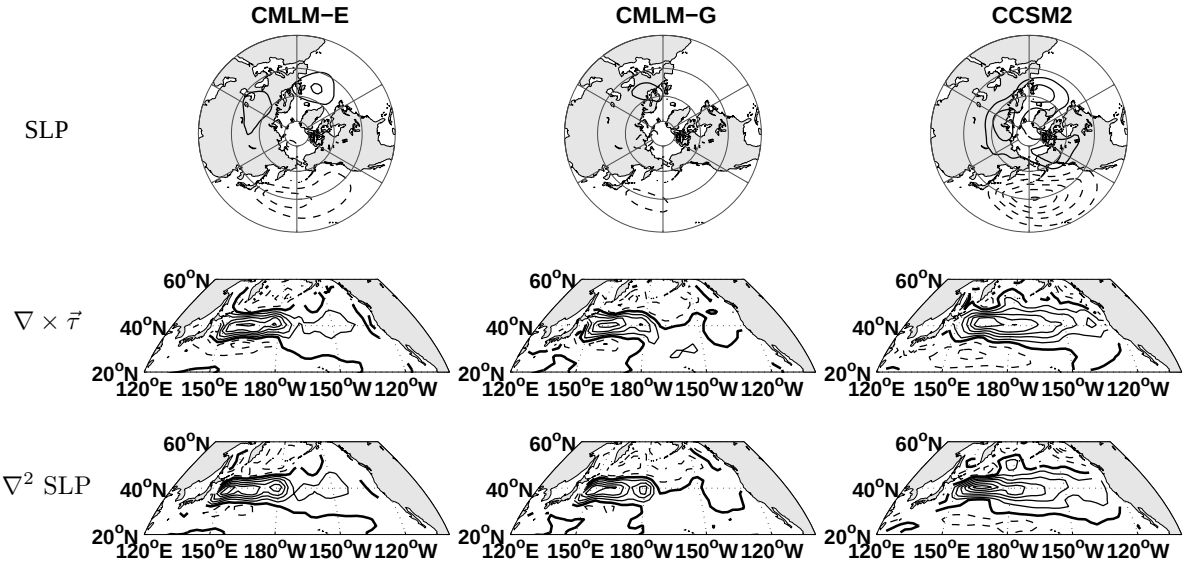

Figure 11: JFM responses for (*top row*) sea-level pressure, (*middle row*) wind stress curl, and (*bottom row*) laplacian of sea-level pressure from (*left column*) CMLM-E, (*center column*) CMLM-G, and (*right column*) CCSM2. The CCSM2 responses are scaled by the ratio between the standard deviation of CCSM2 and CMLM-E SST anomalies averaged in the Kuroshio Extension. Positive (negative) responses are plotted with solid (dashed) contours. Zero contours are suppressed in the sea-level pressure plots. Contour intervals are 1 hPa, 2×10^{-8} N m^{-3}, and 1.5×10^{-12} hPa m^{-2}, respectively.